

A Grid of Synthetic Spectra for Subdwarfs: Non-LTE line-blanketed atmosphere models

THAYSE A. PACHECO,¹ MARCOS P. DIAZ,¹ RONALDO S. LEVENHAGEN,² AND PAULA R. T. COELHO¹

¹*Universidade de São Paulo, Instituto de Astronomia, Geofísica e Ciências Atmosféricas, Rua do Matão, 1226 São Paulo, SP 05508-900, Brazil*

²*Universidade Federal de São Paulo, Departamento de Física, Rua Prof. Artur Riedel, 275, CEP 09972-270, Diadema, SP, Brazil*

(Received April 4th, 2021; Accepted September 7th, 2021)

Submitted to ApJS

ABSTRACT

A new grid of detailed atmosphere model spectra for hot and moderately cool subdwarf stars is presented. High-resolution spectra and synthetic photometry are calculated in the range from 1000 Å to 10,000 Å using Non-LTE fully line-blanketed atmosphere structures. Our grid covers eight temperatures within $10,000 \leq T_{\text{eff}} [\text{K}] \leq 65,000$, three surface gravities in the range $4.5 \leq \log g [\text{cgs}] \leq 6.5$, two helium abundances matching two extreme helium-rich and helium-poor scenarios, and two limiting metallicity boundaries regarding both solar ($[\text{Fe}/\text{H}] = 0$) and Galactic halo ($[\text{Fe}/\text{H}] = -1.5$ and $[\alpha/\text{Fe}] = +0.4$). Besides its application in the determination of fundamental parameters of subdwarfs in isolation and in binaries, the resulting database is also of interest for population synthesis procedures in a wide variety of stellar systems.

Keywords: techniques: spectroscopic — stars: atmospheres — line: profiles — stars: subdwarfs — stars: fundamental parameters

1. INTRODUCTION

The evolutionary scenario of subdwarfs is still emerging. Hot subdwarf stars evolve from low- to intermediate-mass progenitors and reach far beyond the main sequence, at the blue end of the horizontal branch (HB) or mixed with post-HB stars (Heber 2009). Even though they lie mostly between the main sequence and the white dwarf (WD) cooling sequence in the Hertzsprung-Russell diagram, they are contaminated with WDs.

The most accepted formation scenario is of an extreme HB star that lost its envelope after the He-burning phase, evolving directly to the WD-cooling sequence by avoiding the asymptotic giant branch (AGB) (Wade et al. 2005; Heber 2009; Fontaine et al. 2012). These objects experienced mass transfer followed by common envelope ejection in a binary system leaving the stellar core exposed (Green et al. 2008; Geier et al. 2010). More recent investigations support this scenario, such as the

observational evidence of hot O- and B-type subdwarf formation (sdO and sdB, respectively) from the product of binary interactions (Pelisoli et al. 2020). Also, the expected evolutionary path suggests that sdOs evolve from sdBs (Heber 2009). An alternative evolutionary scenario suggests that the merger of two low-mass He-core WDs might form isolated H-rich B-type hot subdwarfs (Hall & Jeffery 2016; Schwab 2018).

A small fraction of sdBs in close binaries (Wade et al. 2005) fall out of the red giant branch before He ignition, perhaps because they are low-mass stars that do not support the burning of He in their cores (Heber 2009).

The hot subdwarfs can be separated into three main groups according to Saffer et al. (2001). i) Those nonbinaries that have no detectable spectral lines from a cool companion, and show only small or insignificant velocity variations (35%). ii) Those single-lined spectroscopic binaries which have significant or large velocity variations and probable orbital periods on the order of a day (45%). iii) Those showing additional spectral lines from a cool FGK main-sequence or subgiant companion that have slowly varying or nearly constant velocities, indicating periods of many months to years.

There is observational evidence indicating that subdwarfs are the most likely candidates to account for the ultraviolet (UV) upturn observed on spectroscopic and photometric analyses of globular clusters and elliptical galaxies (Yi et al. 1999; Busso et al. 2005; Green et al. 2008).

Analysis from asteroseismology (Charpinet et al. 2005), spectroscopy (Wade et al. 2005; Dorsch et al. 2018, 2019), and photometry (Johnson et al. 2014) of field subdwarf stars found nonsolar He abundances. He-rich and He-poor sequences, as a function of effective temperature, were proposed by Edelman et al. (2003) and updated by Németh et al. (2012) and Lei et al. (2019). Those sequences also support the evidence that He-enriched sdOs are more common than the He-deficient ones (Heber 2009).

It is ideal to have homogeneous and widely available model spectra for these elusive systems, in order to improve our knowledge of their fundamental physical parameters and evolution. Such models should be computed as fully as possible regarding the radiative transfer, considering non-local thermodynamic equilibrium (NLTE), fully blanketed atmosphere structures (Lanz & Hubeny 1995; Lanz et al. 1997).

Considerable improvements in NLTE atmosphere models have been achieved over the last five decades. The first NLTE spectra of hot atmospheres in the early 1970s (Mihalas & Hummer 1974) were built based on pure H atmosphere structures, and the metal lines were considered only in the spectral synthesis. Analysis by Lanz & Hubeny (1995) took H, C, and Fe into account for the opacity of hot and high-gravity NLTE atmosphere models. They found critical differences in effective temperature determinations and line profiles arising from the inclusion of explicit atomic species (i.e. with the kinetic equilibrium equation solved) in the atmospheric structure. The subdwarfs' atmospheres have more evident NLTE effects due to their lower surface gravities (when compared to WDs; Lanz et al. 1997). They built spectra considering full line blanketing with H/He, CNO, Si, Fe, and Ni as implicit ions and concluded that this approach significantly improved the line profile analysis. Hubeny et al. (1998) showed that NLTE metal-line-blanketing effects produce a conspicuous difference (typically 20%) in the line profiles seen in the UV spectra of hot WDs. By considering explicit metal ions such as H/He, CNO, Si, and Fe in the atmosphere structure a better emergent flux match was achieved.

Overall, the subdwarfs' spectra are built for specific targets and studies. We have hundreds of hot subdwarf stars cataloged (Geier et al. 2017; Heber et al. 2017; Geier et al. 2019; Geier 2020), with their spectral anal-

ysis focused on classification and/or kinematic properties (Luo et al. 2019). A lot of work was done to analyse the He-abundance (Fontaine et al. 2019) sequences (Lei et al. 2019). The sequences also show differences between field subdwarfs and extreme HB subdwarfs in globular clusters (Lei et al. 2020).

NLTE structures and subdwarf spectra were calculated by Nemeth et al. (2014), covering specific temperature and gravity ranges. The opacities of H, He, and a few metal ions were included to compute the atmosphere structure in these models. However, only a small and nonhomogeneous collection of detailed subdwarf model spectra is currently available. High-temperature spectral grids may be also calculated by other codes e.g. the Tübingen NLTE Model Atmosphere package (Rauch et al. 2018)¹.

In this work we present an extensive high-spectral-resolution grid of NLTE synthetic spectra for subdwarfs in the optical and UV. The models are fully line blanketed with H, He, C, N, O, Ne, Mg, Al, Si, S, and Fe as opacity sources (see table 1). We also consider non-solar chemical abundances to better sample the subdwarf parameter space. Low-temperature convective atmospheres were also included in the square grid. The complete grid is available on our SpecModel website² as well as on the SVO's Theoretical Spectra Web Server³ and the Vizier⁴ databases.

Section 2 describes the atmosphere structure models, in particular the differences between the LTE and NLTE assumptions made. Section 3 describes the synthetic spectra, comparing the results with observational data. Section 4 describes the construction of the synthetic magnitudes and their application in color-color diagrams. Section 5 presents the concluding remarks.

2. ATMOSPHERE STRUCTURE

The atmosphere structure models were computed by TLUSTY code v205 and v208 (for convective 10,000 K models; Hubeny 1988; Hubeny & Lanz 2011a). It calculates a self-consistent solution of the equations describing the radiative (or radiative plus convective) transfer and physical state of the atmosphere. The geometry of the model is plane-parallel with homogeneous chemical abundances (Hubeny & Lanz 1995).

¹ <http://dc.zah.uni-heidelberg.de/theossa/q/web/form>

² Spectral Models of Stars and Stellar Populations, <http://specmodels.iag.usp.br/>.

³ Spanish Virtual Observatory, <http://svo2.cab.inta-csic.es/theory/newov2/>.

⁴ <https://vizier.u-strasbg.fr/viz-bin/VizieR>

The most popular subdwarf models available have been built in LTE. In LTE all energy partitioning such as atomic, ionic, and molecular level populations is given by Saha-Boltzmann equations, being defined by the local temperature. The LTE conditions may differ from those derived in actual statistical equilibrium, therefore level populations in NLTE were calculated. Departures from LTE may be specially significant for high-temperature subdwarf atmospheres (Hubeny & Lanz 1995; Lanz & Hubeny 1995; Lanz et al. 1997) as also found in DA-type WD atmospheres (Levenhagen et al. 2017).

The starting point was to compute a LTE gray structure model, which is then used as an input to build the NLTE line-blanketed models (Hubeny 1988; Hubeny et al. 1994). We considered H, He, C, N, O, Ne, Mg, Al, Si, S, and Fe as explicit ions (see table 1) contributing to the opacity. The set of ionization states for the selected atomic species were chosen on the basis of ionization energies, model-effective-temperatures and candidate-permitted transitions from Williams & Livio (1995). The atomic data of each ion included as an explicit species in the NLTE atmosphere models are summarized in table 1 (see details in Lanz & Hubeny 2003, Lanz & Hubeny 2007).

As described by Lanz & Hubeny (2007), the LTE fluxes are about 10% higher than the NLTE predictions, and this is most noticeable in the near-UV. Lanz & Hubeny (2007) also mentioned that the lower NLTE fluxes result from the overpopulation of the H I ($n = 2$) level at the depth of formation of the continuum flux, hence implying a larger Balmer continuum opacity.

The adopted abundances are expressed as solar ($[\text{Fe}/\text{H}] = 0.0$; Asplund et al. 2009) or Galactic halo ($[\text{Fe}/\text{H}] = -1.5$ and $[\alpha/\text{Fe}] = +0.4$) as well as He-rich (Edelmann et al. 2003) and He-poor abundances (Németh et al. 2012; Lei et al. 2019). Our choice of using solar and halo metallicity is not intended to describe subdwarf typical abundances. Instead, these solar and halo points just set a broad Z range, probing its effect on the continuum and line profiles. It is well established that atmospheric subdwarf metal abundances have little or virtually no memory of their parent main sequence abundances (e.g. Moehler 2001; Németh et al. 2012; Byrne et al. 2018). Metals at the subdwarf surface vary by large amounts depending on previous binary evolution and diffusion processes, leading to diverse abundance patterns (e.g. O’Toole & Heber 2006) with loose observational constraints. He-rich and He-poor abundance variations were chosen based on linear fits as a function of temperature based on Lei et al. (2019) (see table 2). Note that TLUSTY (Hubeny 1988; Hubeny & Lanz 2011a) uses the solar chemical abundances as de-

finied by Grevesse & Sauval (1998) as default values, and we rearranged all the chemical species to the solar abundance as defined by Asplund et al. (2009). The atmosphere structures (available upon request to the authors) may be interpolated in metallicity and specific modified metal abundances used in custom spectral synthesis.

The time spent on computational work increases and the convergence is more difficult when the complexity of the heavy elements is included in the TLUSTY atmosphere code (Hubeny 1988; Hubeny & Lanz 2011a). As a reference, each one of the 96 structures were computed and analyzed in a typical time scale of a day.

The grid of subdwarf-structure models is composed of eight effective temperatures (T_{eff} : 10,000, 15,000, 20,000, 25,000, 30,000, 35,000, 45,000, and 65,000 K), each one computed in three surface gravities ($\log g$ [cgs]: 4.5, 5.5, and 6.5) and four different chemical abundances: solar and He-rich, solar and He-poor, halo and He-rich, halo and He-poor.

The broadening of lines was treated carefully considering the Lyman and Balmer line profile tables from Tremblay & Bergeron (2009). The high-frequency limit for lines that are taken into account in the opacity sampling was set to $6 \times 10^{11} \times T_{\text{eff}}$ or the highest bound-free edge frequency, if greater. Opacity-sampling steps smaller than the thermal broadening were set. The microturbulent velocity was set to 10 km s^{-1} . The opacity-sampling approach was used to compute the superline cross sections with better accuracy, also, the iron peak lines were treated in a line-blanketed model.

The only exception to the description above was the cooler atmosphere models with 10,000 K which require a convective treatment (Fontaine et al. 1981; Bergeron et al. 1992); a mixing-length theory parameter equal to the pressure-scale height ($\alpha_{\text{MLT}} = 1.0$) was used. For the 10,000 K case, the final structure model was computed in LTE without a microturbulent velocity.

Most models were computed using the hybrid complete-linearization and accelerated lambda-iteration (CL/ALI) method (Hubeny & Lanz 1995; Hubeny 2003), which is the default procedure for computing fully consistent, NLTE metal-line-blanketed atmosphere models in TLUSTY (Hubeny 1988). When the convergence was not achieved directly from CL/ALI we computed the atmosphere structure models using the Rybicki scheme (Hubeny & Mihalas 2014), which is also suitable for treating high-temperature and high-gravity atmospheres, with better convergence behavior in some cases.

The effective temperature as function of the mass depth is shown in figure 1. The outermost mass depth corresponds to the Rosseland optical depth $\tau = 10^{-7}$

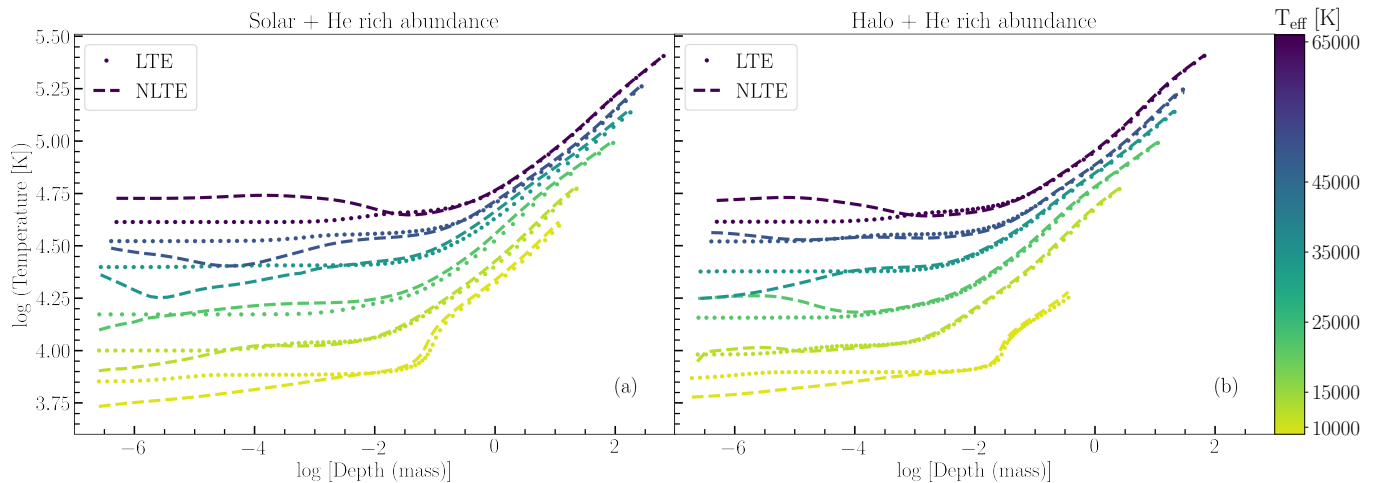


Figure 1. Structure models of the temperature [K] as function of mass depth [g cm^{-2}] in a logarithmic scale computed using LTE (dotted lines) and NLTE (dashed lines) assumptions. The effective temperatures are shown in the colored scale from bottom (10,000 K) to top (65,000 K). a) These models have solar and He-rich abundances and $\log g$ [cgs] = 4.5. b) These models have halo and He-rich abundances and $\log g$ [cgs] = 6.5.

while the innermost depth has $\tau = 100$, logarithmically sampled in 70 layers. The color-bar scale indicates the effective temperature from bottom 10,000 K in yellow to top 65,000 K in purple. The hottest structures are more extended toward the inner thick region compared to the coolest model. The structure models in figure 1 (a) have a surface gravity ($\log g$) equal to 4.5, so they are more extended if we compare them to the structures in figure 1 (b), which represent more compact objects with $\log g$ equal to 6.5. The dotted lines represent the starting model computed using LTE assumptions, where we can see the almost isothermal behavior in the external region for models with different effective temperatures. On the other hand, the dashed lines represent the structure computed using the NLTE assumptions and line blanketing of the explicit species. In the latter, a small temperature inversion on their outer regions can be seen in some cases, which is important to the line-core profile formation. The inner region converges to the solution with minor differences if we compare the LTE and NLTE structures. Note that mass depths are shown, if we look at a specific line optical depth the differences between LTE and NLTE structure models are much more significant.

The structure models are highly sensitive to the chemical abundances via opacities, electron density, and mass density. The explicit atoms and ions included to compose the level and superlevels are the most important ingredients to compute detailed NLTE structure models. They have an impact on the cross section computation, justifying the careful choice of the most important ions for each model.

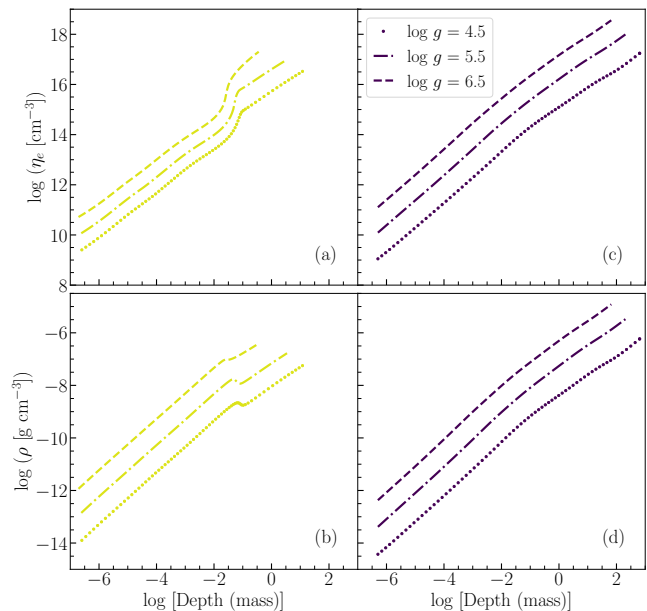


Figure 2. Structure models of the electron density (top) and mass density (bottom) as function of mass depth [g cm^{-2}] in a logarithmic scale. We are comparing different surface gravity models computed using NLTE assumptions. These models have halo and He-rich abundances. a), b) $T_{\text{eff}} = 10,000$ K; c), d) $T_{\text{eff}} = 65,000$ K.

The electron density and the mass density are shown in figure 2, having a similar profile as a function of the mass depth. The effects of the surface gravity in the atmosphere height are evident as already mentioned above. The coolest structure models such as the example of 10,000 K in figure 2 a) and b) have an inversion on the density profiles near $\log [\text{Depth (mass)}] = -1$, this is due to the effect of convection that was considered for

Table 1. Atomic data of the explicit species included in the NLTE atmosphere models

ATOMIC DATA				EXPLICIT IONS INCLUDED IN NLTE							
Ion	Super(level)	Lines	Reference	10 kK	15 kK	20 kK	25 kK	30 kK	35 kK	45 kK	65 kK
H ⁻	1	1	1	✓	✓	✓					
H	9	172	1	✓	✓	✓	✓	✓	✓	✓	✓
He	24	784	2	✓	✓	✓	✓	✓	✓	✓	✓
He II	20	190	1	✓	✓	✓	✓	✓	✓	✓	✓
C	40	3,201	3	✓	✓	✓	✓				
C II	22	238	4	✓	✓	✓	✓	✓	✓	✓	✓
C III	46	738	5	✓	✓	✓	✓	✓	✓	✓	✓
C IV	25	330	6				✓	✓	✓	✓	✓
N	34	785	1	✓	✓	✓	✓				
N II	42	3,396	3	✓	✓	✓	✓	✓	✓	✓	✓
N III	32	549	4	✓	✓	✓	✓	✓	✓	✓	✓
N IV	48	1,093	5				✓	✓	✓	✓	✓
N V	16	330	6				✓	✓	✓	✓	✓
O	33	418	1	✓	✓	✓	✓				
O II	48	3,484	1	✓	✓	✓	✓	✓	✓	✓	✓
O III	41	3,855	3		✓	✓	✓	✓	✓	✓	✓
O IV	39	922	4				✓	✓	✓	✓	✓
O V	6	4	4				✓	✓	✓	✓	✓
Ne	35	2,715	7	✓	✓	✓	✓				
Ne II	32	2,301	1	✓	✓	✓	✓	✓	✓	✓	✓
Ne III	34	1,354	1				✓	✓	✓	✓	✓
Ne IV	12	38	1				✓	✓	✓	✓	✓
Mg II	25	306	1	✓	✓	✓	✓	✓	✓	✓	✓
Al II	29	536	8	✓	✓	✓	✓	✓	✓	✓	✓
Al III	23	306	1	✓	✓	✓	✓	✓	✓	✓	✓
Si II	40	392	9	✓	✓	✓	✓				
Si III	30	747	8	✓	✓	✓	✓	✓	✓	✓	✓
Si IV	23	306	1		✓	✓	✓	✓	✓	✓	✓
S II	33	4,166	1	✓	✓	✓	✓				
S III	41	3,452	10	✓	✓	✓	✓	✓	✓	✓	✓
S IV	38	909	9		✓	✓	✓	✓	✓	✓	✓
S V	25	1,171	8				✓	✓	✓	✓	✓
S VI	16	398	1							✓	✓
Fe II	36	1,264,969	12, 13	✓	✓	✓	✓				
Fe III	50	1,604,934	11, 13	✓	✓	✓	✓	✓	✓	✓	✓
Fe IV	43	1,776,984	11, 14		✓	✓	✓	✓	✓	✓	✓
Fe V	42	1,008,835	11, 15				✓	✓	✓	✓	✓
Fe VI	32	40,298	11, 15					✓	✓	✓	✓

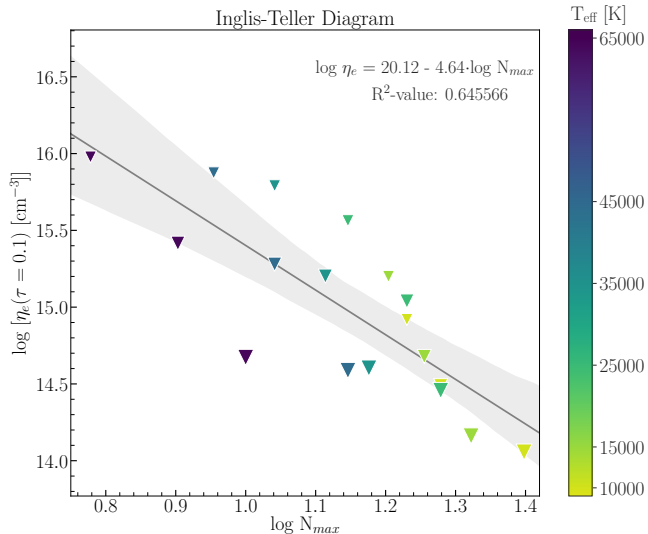
References: (1) Lanz & Hubeny 2003, 2007; (2) <http://physics.nist.gov/PhysRefData/ASD/index.html>; (3) Luo & Pradhan 1989; (4) Fernley et al. 1999; (5) Tully et al. 1990; (6) Peach et al. 1988; (7) Hibbert & Scott 1994; (8) Butler et al. 1993; (9) Mendoza et al. 1995; (10) Nahar & Pradhan 1993; (11) Kurucz 1994; (12) Nahar 1997; (13) Nahar 1996; (14) Bautista & Pradhan 1997; (15) Bautista 1996.

Table 2. Numerical He Abundances

T_{eff} [K]	$\log(n_{\text{He}}/n_{\text{H}})_{\text{poor}}$	$\log(n_{\text{He}}/n_{\text{H}})_{\text{rich}}$
10,000	-4.98	-3.81
15,000	-4.35	-3.13
20,000	-3.72	-2.46
25,000	-3.09	-1.78
30,000	-2.46	-1.11
35,000	-1.83	-0.43
45,000	-0.57	0.92
65,000	1.95	3.62

these specific temperatures. The hot structure models as the example of 65,000 K in figure 2 c) and d) have densities with a linear dependency of the mass depth.

An Inglis-Teller diagram for the grid was produced, which is a classical tool for evaluating model sequences' behavior over a gravity range. It involves the electron density and the maximum n level that originates a distinguishable Balmer absorption line, which is useful for diagnosing our model's quality. We interpolated the model electron density to a specific optical depth $\tau = 0.1$, counting the highest visible term in the final synthetic spectra. A linear least-squares fit of the electron density, and the maximum number of the absorption lines near the Balmer's discontinuity, is shown in figure 3.

**Figure 3.** An Inglis-Teller diagram of models with halo and He-rich abundances.

We also performed convergence analyses for all the 96 subdwarf-structure models computed. The most critical convergence criterion is the magnitude of the relative changes of the components of the state vector, which is defined as a set of all structural parameters (e.g. tem-

perature, particle number densities, and the mean radiation intensities in discretized frequency points) in a given discretized depth point (Hubeny & Lanz 2011a). The necessary condition for convergence is that the maximum relative change of all state vector components in all the 70 depths is smaller than 10^{-3} . However, a supplementary condition is the conservation of the total flux concerning the total theoretical flux, σT_{eff}^4 . The output parameters such as the number of depths, column mass, temperature, and densities in each depth and relative changes between iterations are used in the convergence analysis, as well as in the emergent flux in all frequency points used by the SYNSPEC code (Hubeny & Lanz 2011b) to build synthetic spectra.

3. SYNTHETIC SPECTRA

We computed the grid of synthetic spectra with the SYNSPEC code designed to synthesize the emergent spectra from atmosphere model structures. We used the NLTE atmosphere structure from TLUSTY models (Hubeny 1988; Hubeny & Lanz 2011a) described in section 2. We considered NLTE assumptions for the evaluation of the level and superlevel populations. The line profiles were carefully treated in a special computation for H and He (Lanz & Hubeny 2003, 2007). The reference atomic line list is Coelho (2014), based on Coelho et al. (2005) and line lists from R. Kurucz⁵ and F. Castelli⁶ (see, e. g. Kurucz 2017; Castelli & Hubrig 2004).

The hydrogen and hydrogenic lines are treated as a part of the continuum and their profiles are computed using tables from Tremblay & Bergeron (2009). The quasi-molecular satellites of $L\alpha$, $L\beta$, and $H\alpha$ ($\lambda = 1215.67$, 1025.18 and 6562.79 Å, respectively), are considered. In that case, additional input files containing the corresponding data were used (Allard et al. 2009).

The four He I triplet lines, ($\lambda = 4026$, 4387 , 4471 , and 4921 Å) were treated using special line-broadening tables (Barnard et al. 1974; Shamey 1969). The He II lines are treated as the approximate hydrogenic ion by analytical values of the Stark + Doppler profile (Hubeny et al. 1994), which improves the accuracy of the line profile for $T_{\text{eff}} > 10,000$ K, and the line profiles are given by the Stark-broadening tables of Schöning & Butler (1989). We are also considering Stark broadening computed by Tremblay & Bergeron (2009).

The spectral grid coverage is between 1000 - 10,000 Å with steps of 0.01 Å. The resulting spectrum was subsequently processed with the ROTIN code (Hubeny & Lanz

⁵ <http://kurucz.harvard.edu/linelists.html>

⁶ <http://wwwuser.oats.inaf.it/castelli/linelists.html>

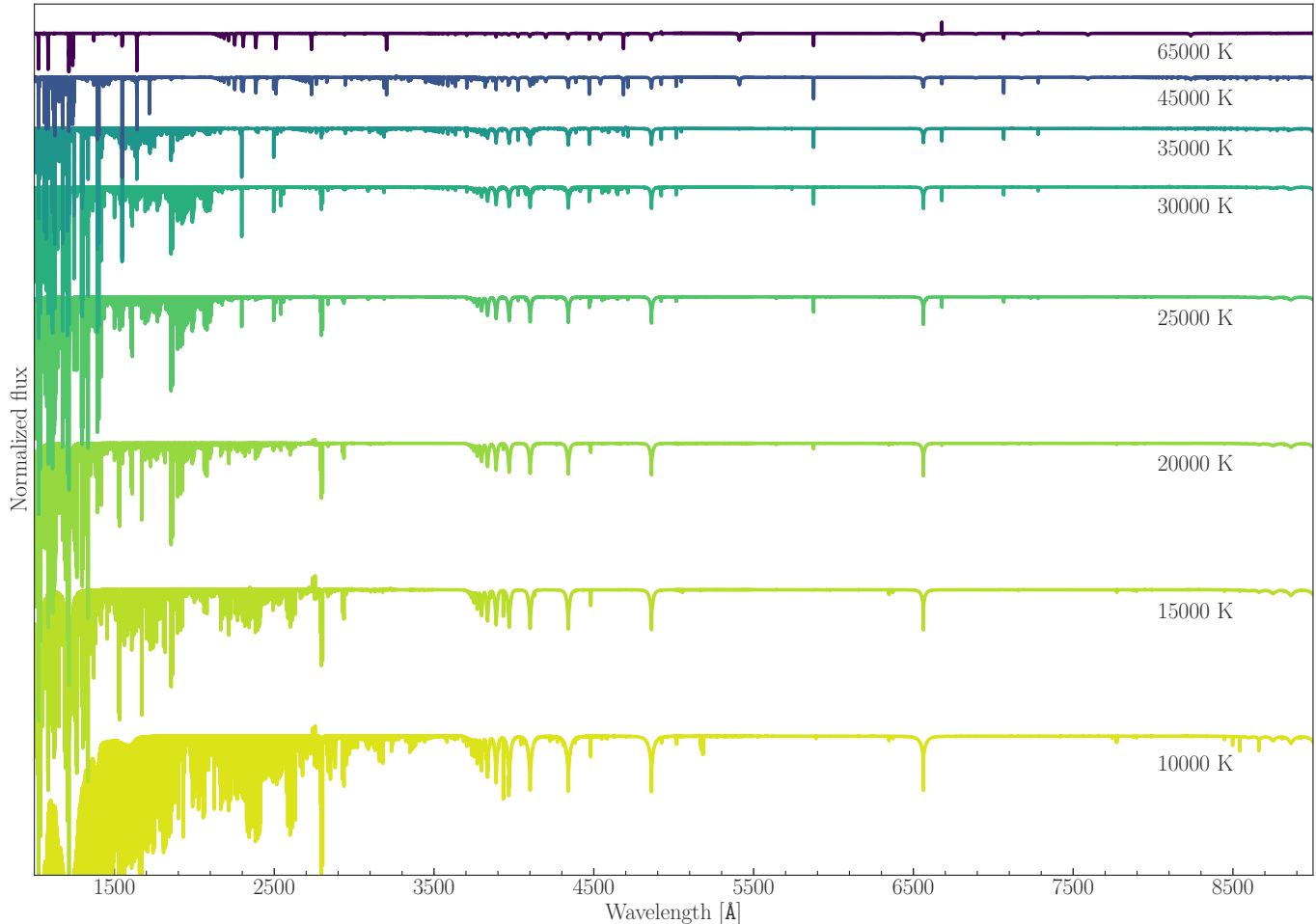


Figure 4. Sample spectra with coverage from 1000 - 9000 Å without instrumental broadening for different temperatures from top (65,000K) to bottom (10,000K), $\log g$ [cgs] = 5.5 with halo and He-rich abundances.

2011b), which resamples the original synthetic spectrum but considering that no rotational velocity and no instrumental degradation have been taken into account.

We show the normalized emergent flux (in arbitrary units) given as a function of wavelength for the spectral coverage from 1000 to 9000 Å in figure 4. A forest of lines is seen at this particular sampling, where no instrumental degradation is included. They are synthetic spectra with T_{eff} equal to 65,000, 45,000, 35,000, 30,000, 25,000, 20,000, 15,000 and 10,000 K (from top to bottom) and $\log g$ [cgs] = 5.5 with halo and He-rich abundances.

In figure 5 we can compare the different spectral types in the near-UV region between 1000 and 2000 Å, where for visual effect it is degraded to a gaussian instrumental profile with full width at half maximum (FWHM) equal to 5 Å. The hotter spectra have a bluer continuum and the He lines are dominant. The Stark broadening is more evident on the coolest spectra, where a stronger Lyman series is present, besides its quasi-molecular absorption features.

In figure 6 we can compare the different spectral types on the Balmer break region between 3500 - 6750 Å, where for visual effect the resolution is degraded by a gaussian instrumental profile with FWHM equal to 5 Å. As expected, the H is mostly ionized and the Balmer series is weaker in the hotter spectra. The coolest models are not favorable to the formation of strong He lines. Moreover, the spectra presented in figure 6 follow the He-abundance sequence from Németh et al. (2012), which shows low He abundance even for the He-rich sequence of cool subdwarfs.

With the purpose of illustrating the grid, we present a simple comparison of model spectra with the spectra of the Lamost 442708048, Lamost 183405148, and HD 4539 subdwarfs. No interpolation in the grid was performed as the intent is not to determine exact abundances or stellar parameters, but rather to exhibit the grid potentialities. The targets were selected from the subdwarf catalog in Lei et al. (2019) and Hubble Space Telescope’s (HST)/Space Telescope Imaging Spectrograph

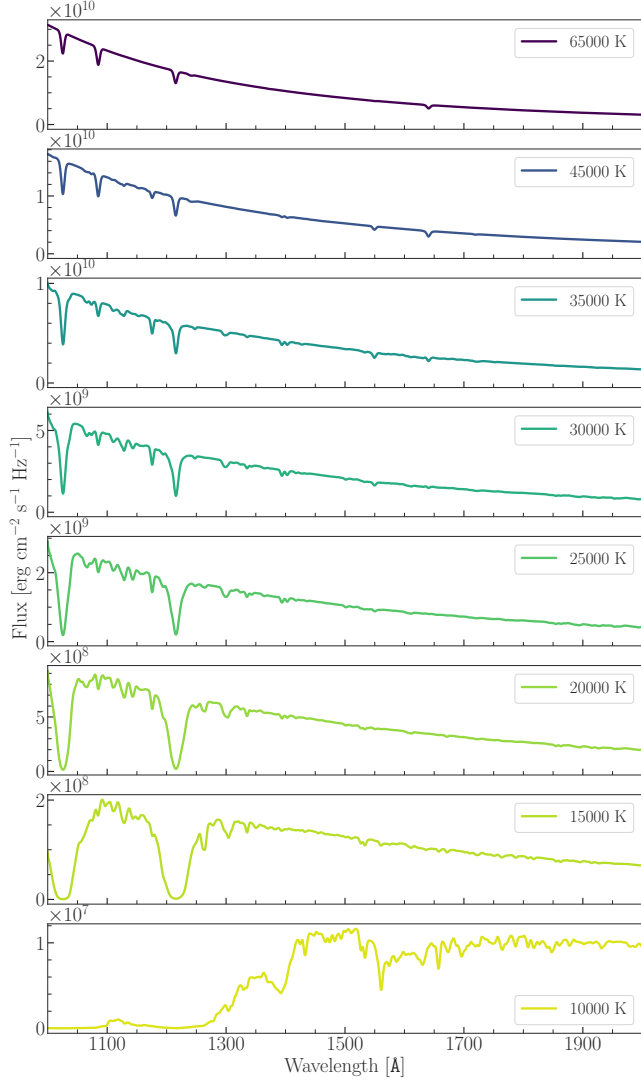


Figure 5. Sample spectra in the UV region (1000 - 2000 Å) with FWHM resolution = 5 Å for different temperatures: from top (65,000K) to bottom (10,000K), and $\log g$ [cgs] = 5.5 with halo and He-rich abundances.

(STIS) Legacy Archive data. They are located in the solar neighborhood.

According to [Lei et al. \(2019\)](#), the target Lamost 442708048 has $T_{\text{eff}} = 26,620 \pm 70$ K, $\log g = 5.53 \pm 0.01$ [cgs], $\log (n_{\text{He}}/n_{\text{H}}) = -2.78 \pm 0.05$, $E(B - V) = 0.018$ and, from the [Gaia Collaboration et al. \(2018\)](#) parallax, its distance is 317 ± 5 pc. We performed a comparison with models near to these values, within the boundaries of our grid, as $T_{\text{eff}} = 25,000$ K, $\log g = 5.5$ [cgs], $[\text{Fe}/\text{H}] = 0$, and $\log (n_{\text{He}}/n_{\text{H}}) = -3.09$ (see figure 7 (a)).

Lamost 183405148 has, according to [Lei et al. \(2019\)](#), $T_{\text{eff}} = 46,270 \pm 330$ K, $\log g = 5.88 \pm 0.04$, $\log (n_{\text{He}}/n_{\text{H}}) = 0.29 \pm 0.01$, $E(B - V) = 0.021$, and from its parallax ([Gaia Collaboration et al. 2018](#)) the distance is 333 ± 9

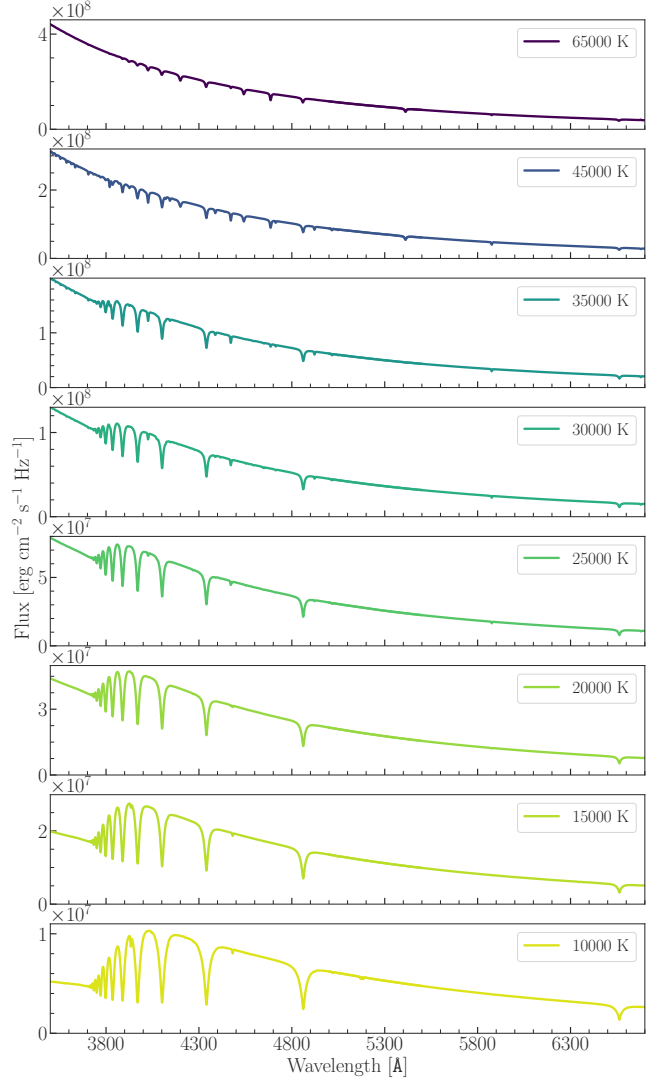


Figure 6. Sample spectra in the optical region (3500 - 6750 Å) with FWHM resolution = 5 Å for different temperatures: from top (65,000K) to bottom (10,000K), and $\log g$ [cgs] = 5.5 with halo and He-rich abundances.

pc. The closest model spectrum adopted corresponds to $T_{\text{eff}} = 45,000$ K, $\log g = 5.5$ [cgs], $[\text{Fe}/\text{H}] = 0$, and $\log (n_{\text{He}}/n_{\text{H}}) = 0.92$ (see figure 7 (b)).

HST/STIS Legacy Archive data on the bright subdwarf HD 4539 were used to illustrate the models in the FUV. Parameters for this sdB are as follows: $T_{\text{eff}} = 26,000 \pm 500$ K, $\log g = 5.2 \pm 0.1$, $\log (n_{\text{He}}/n_{\text{H}}) = -2.32 \pm 0.05$, $E(B - V) = 0.04 \pm 0.01$ ([Sale et al. 2008](#)) and $d = 171.6 \pm 2.1$ pc ([Gaia EDR3; Gaia Collaboration et al. \(2021\)](#)). The models were scaled to match the continuum flux in the middle of each spectral range. He-poor branch and halo low-Z abundances were assumed here while T_{eff} and $\log g$ were linearly interpolated from model nodes to the literature values (see figure 8). Rota-

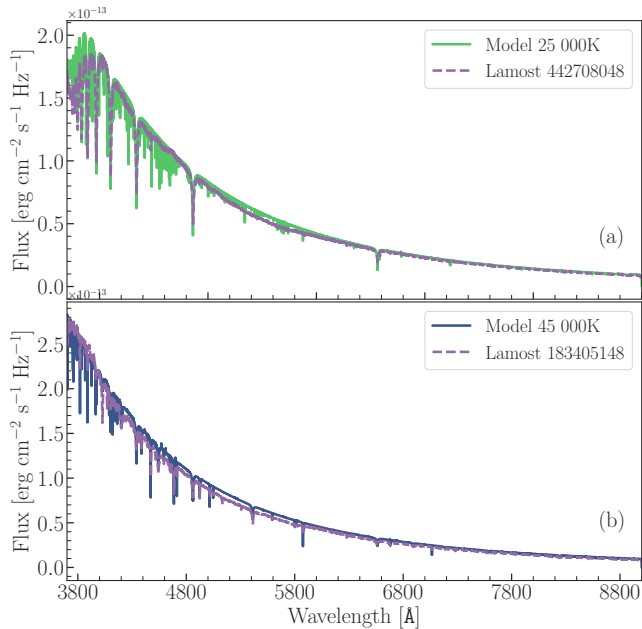


Figure 7. Top: comparison between the observed spectrum of subdwarf Lamost 4427080 (dashed purple) and the model spectrum with $T_{\text{eff}} = 25,000$ K and $\log g = 5.5$ (solid green). Bottom: comparison between the observed spectrum of Lamost 183405148 (dashed purple) and the model spectrum with $T_{\text{eff}} = 45,000$ K and $\log g = 5.5$ (solid blue).

tion, instrumental resolution, and exact chemical composition were neglected, which would explain the significant differences found in the lines and continua offsets. By using the Gaia distances and reddening values above, stellar radii compatible with typical values for subdwarfs in eclipsing binaries (e.g. Rebassa-Mansergas et al. (2019)) could be found. A line and/or continuum fitting of spectra can be performed with the XTGRID facility (Nemeth 2019).

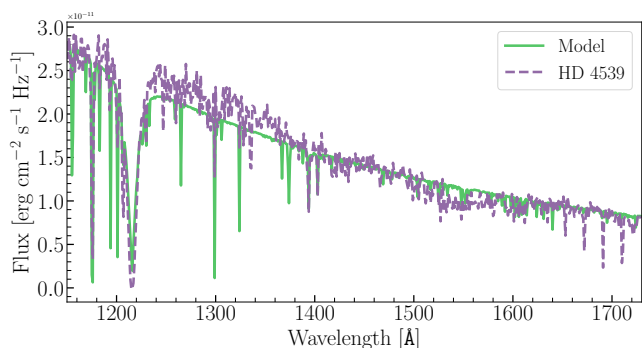


Figure 8. Comparison between the observed HST/STIS UV spectrum of HD 4539 (dashed purple) and an interpolated model spectrum with $T_{\text{eff}} = 26,000$ K and $\log g = 5.2$ (solid green).

4. SYNTHETIC MAGNITUDES

Synthetic magnitudes have been computed for several standard photometric bands to trend the grid’s behavior in the color indices space and provide a comparison with photometry data. We used the filter response functions available on the Filter Profile Service at the Spanish Virtual Observatory ⁷ to convolve our synthetic integrated fluxes in the AB and Vega systems. The filters were interpolated in the spectra wavelength steps within the Shannon-Whittaker scheme. Photon-counting integrated fluxes were assumed (Bessell et al. 1998). Vega’s zero-points were previously evaluated from Calspec’s standard spectrum (Bohlin et al. 2014).

Figure 9 illustrate our models in two color-color panels: panel (a) was chosen to trace the overall continuum inclination, and panel (b) traces the behavior of the Balmer jump. In panel (a) we show F469N - F673N versus FQ757N - FQ750N colors of the HST/Wide Field Camera 3 (WFC3) photometric system. The dependence on effective temperature is clear. Those indices measure how lower-temperature synthetic models have a flatter continuum in the optical region. The point-size scale represents the surface gravity, where larger symbols relate to lower gravity ($\log g = 4.5$), and smaller symbols stand for higher gravity ($\log g = 6.5$), which also reveal a linear dependence in the color space. Finally, the circles represent solar abundance and down-pointing triangles represent low halo metallicity, which has no clear separation on the diagram.

In figure 9 (b) the Strömgren photometric system indices were used. Zero-points were derived from Vega *ubvy* magnitudes (Hauck & Mermilliod 1998) and its calibrated spectrum from the STScI CALSPEC database (Bohlin et al. 2014). The color-color diagram of figure 9 (b) was constructed with u (349.6nm) - v (410.3nm) and $v - b$ (466.6nm) colors. It shows a temperature dependence of the Balmer break, which is more evident and also gravity-dependent for cooler atmospheres.

The study of the 5874 hot subdwarf stars with Gaia Data Release 2 by Geier 2020 is the most complete sample of subdwarfs. From this catalog we selected data from 3450 targets (1482 with determined effective temperature and colors) observed by the Sloan Digital Sky Survey (SDSS) photometric system to compare with the grid synthetic magnitudes. The color-color diagram in figure 10 is composed of $g - r$ and $u - g$ colors without any color cutoff. Observational data with a determined effective temperature are shown as dots scaled by hue, while those with an undetermined effective temperature

⁷ <http://svo.cab.inta-csic.es/main/index.php>

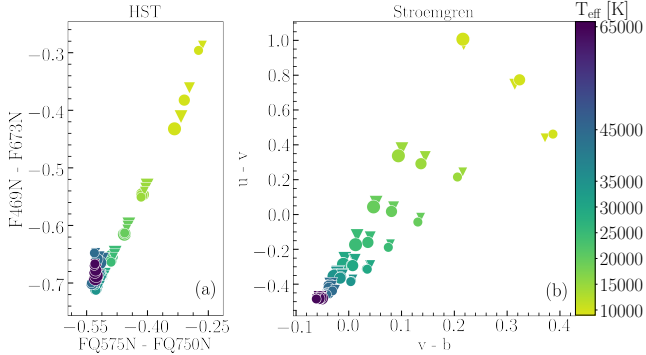


Figure 9. Color-color diagrams with the scale showing the effective temperatures, while the point-size scale shows the surface gravities (larger to lower gravity (4.5) and smaller to the higher gravity (6.5)); the circles indicate solar abundances and down-pointing triangles the low halo metallicity. (a) Color-color diagram for HST/WFC3 indices F469N - F673N and FQ757N - FQ750N. (b) Color-color diagram for classical Strömgren u (349.6nm) - v (410.3nm) and $v - b$ (466.6nm) indices, aiming to probe the Balmer discontinuity.

are gray crosses. Our synthetic colors are displayed in the same hue, style, and size scales as in figure 9, matching the sdO, sdB, and sdOB previously classified by Geier 2020. The upper data sequence represents the subdwarf composite binaries with main-sequence stars companions.

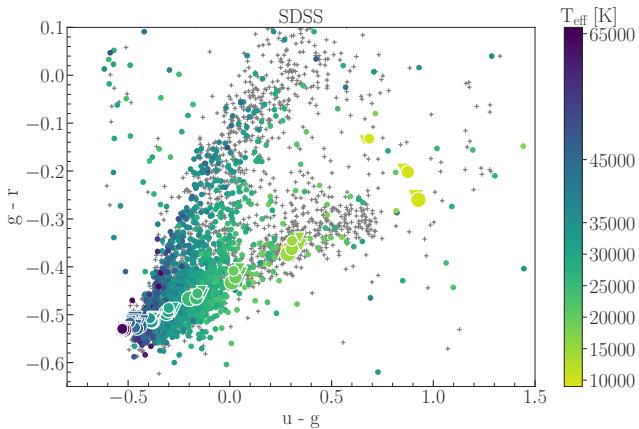


Figure 10. Color-color diagram ($g - r$ vs. $u - g$) composed of observational data on subdwarfs from SDSS (see text) with a hue scale representing determined effective temperatures, while the gray crosses shown an undetermined effective temperature. The synthetic colors from our grid are plotted with the same hue, style, and size scales as in figure 9.

5. SUMMARY

We presented a grid of NLTE, fully blanketed theoretical spectra and synthetic photometry for hot and

moderately cool subdwarf stars. The atmosphere models were computed considering line blanketing of H, He, C, N, O, Ne, Mg, Al, Si, S, and Fe. The effective temperatures are $T_{\text{eff}} = 10,000, 15,000, 20,000, 25,000, 30,000, 35,000, 45,000,$ and $65,000$ K, while the surface gravities are $\log g [\text{cgs}] = 4.5, 5.5,$ and 6.5 . The two representative chemical abundances are solar and Galactic halo, each one with two extreme scenarios for He-rich and He-poor stellar atmospheres.

The main differences between LTE and NLTE atmosphere structures are shown for these objects. They have significant differences in the outermost atmospheres, leading to distinct line-core profile formation.

The complete high-resolution spectral synthesis is performed from the UV to near-IR (1000 to 10,000 Å) in 0.01 Å steps. We provided an illustrative analysis for the UV and the optical regions by comparing our models with observed spectra from LAMOST and HST/STIS Legacy Archive data.

The behavior of the color indices were analyzed using the HST/WFC3 and the Strömgren photometric systems. A clear separation in effective temperature can be seen, as well as gravity for lower-temperature models, as provided by the Balmer discontinuity. We also matched our synthetic magnitudes against SDSS subdwarf data with fair agreement.

These results pave the way for both spectroscopic and photometric analyses of fundamental parameters in isolated or binary objects which, in turn, may provide a more detailed insight into the atmosphere models themselves. In addition, classical stellar population synthesis analysis can make use of the homogeneous spectral grid to better understand the blue and UV properties of old stellar populations. The full spectral grid and synthetic indices are available in the IAG-USP², SVO³, and Vizier⁴ databases.

ACKNOWLEDGMENTS

We thank Ivan Hubeny who kindly released the new versions of TLUSTY 208 and SYNPEC 54 and boosted the discussions about the convective models. We thank the anonymous referee for refereeing this paper and for the suggestions that improved the work.

This study was financed in part by the Coordenação de Aperfeiçoamento de Pessoal de Nível Superior - Brasil (CAPES), Finance Code 001. M.P.D. acknowledges support from CNPq under grant #305033. P.C. acknowledges support from Conselho Nacional de Desenvolvimento Científico e Tecnológico (CNPq) under grant #310041/2018-0 and from Fundação de Amparo

à Pesquisa do Estado de São Paulo (FAPESP) process #2018/05392-8.

This research has made use of the SVO Filter Profile Service (<http://svo2.cab.inta-csic.es/theory/fps/>) supported from the Spanish MINECO through grant AYA2017-84089. This work has made use of

data from the European Space Agency (ESA) mission *Gaia* (<https://www.cosmos.esa.int/gaia>), processed by the *Gaia* Data Processing and Analysis Consortium (DPAC; <https://www.cosmos.esa.int/web/gaia/dpac/consortium>). Funding for the DPAC has been provided by national institutions, in particular the institutions participating in the *Gaia* Multilateral Agreement.

REFERENCES

- Allard, N. F., Noselidze, I., & Kruk, J. W. 2009, *A&A*, 506, 993
- Asplund, M., Grevesse, N., Sauval, A. J., & Scott, P. 2009, *ARA&A*, 47, 481
- Barnard, A., Cooper, J., & Smith, E. 1974, *Journal of Quantitative Spectroscopy and Radiative Transfer*, 14, 1025
- Bautista, M. A. 1996, *A&AS*, 119, 105
- Bautista, M. A., & Pradhan, A. K. 1997, *A&AS*, 126, 365
- Bergeron, P., Wesemael, F., & Fontaine, G. 1992, *ApJ*, 387, 288
- Bessell, M. S., Castelli, F., & Plez, B. 1998, *A&A*, 333, 231
- Bohlin, R. C., Gordon, K. D., & Tremblay, P. E. 2014, *PASP*, 126, 711
- Busso, G., Moehler, S., Zoccali, M., Heber, U., & Yi, S. K. 2005, *ApJL*, 633, L29
- Butler, K., Mendoza, C., & Zeippen, C. J. 1993, *Journal of Physics B Atomic Molecular Physics*, 26, 4409
- Byrne, C. M., Jeffery, C. S., Tout, C. A., & Hu, H. 2018, *MNRAS*, 475, 4728, doi: [10.1093/mnras/sty158](https://doi.org/10.1093/mnras/sty158)
- Castelli, F., & Hubrig, S. 2004, *A&A*, 425, 263
- Charpinet, S., Fontaine, G., Brassard, P., Green, E. M., & Chayer, P. 2005, *Astronomy and Astrophysics*, 437, 575
- Coelho, P., Barbuy, B., Meléndez, J., Schiavon, R. P., & Castilho, B. V. 2005, *A&A*, 443, 735
- Coelho, P. R. T. 2014, *MNRAS*, 440, 1027
- Dorsch, M., Latour, M., & Heber, U. 2018, *OAst*, 27, 19
- . 2019, *A&A*, 630, A130, doi: [10.1051/0004-6361/201935724](https://doi.org/10.1051/0004-6361/201935724)
- Edelmann, H., Heber, U., Hagen, H. J., et al. 2003, *A&A*, 400, 939
- Fernley, J. A., Hibbert, A., Kingston, A. E., & Seaton, M. J. 1999, *Journal of Physics B Atomic Molecular Physics*, 32, 5507
- Fontaine, G., Bergeron, P., Brassard, P., et al. 2019, *ApJ*, 880, 79
- Fontaine, G., Brassard, P., Charpinet, S., et al. 2012, *A&A*, 539, A12
- Fontaine, G., Villeneuve, B., & Wilson, J. 1981, *ApJ*, 243, 550
- Gaia Collaboration, Brown, A. G. A., Vallenari, A., et al. 2018, *A&A*, 616, A1
- . 2021, *A&A*, 649, A1, doi: [10.1051/0004-6361/202039657](https://doi.org/10.1051/0004-6361/202039657)
- Geier, S. 2020, *A&A*, 635, A193
- Geier, S., Heber, U., Podsiadlowski, P., et al. 2010, *A&A*, 519, A25
- Geier, S., Raddi, R., Gentile Fusillo, N. P., & Marsh, T. R. 2019, *A&A*, 621, A38
- Geier, S., Østensen, R. H., Nemeth, P., et al. 2017, *OAst*, 26, 164
- Green, E. M., Fontaine, G., Hyde, E. A., For, B.-Q., & Chayer, P. 2008, *PASP*, 392
- Grevesse, N., & Sauval, A. J. 1998, *SSRv*, 85, 161
- Hall, P. D., & Jeffery, C. S. 2016, *MNRAS*, 463, 2756
- Hauck, B., & Mermilliod, M. 1998, *A&AS*, 129, 431
- Heber, U. 2009, *ARA&A*, 47, 211
- Heber, U., Irrgang, A., & Schaffenroth, J. 2017, *OAst*, 1, 1
- Hibbert, A., & Scott, M. P. 1994, *Journal of Physics B Atomic Molecular Physics*, 27, 1315
- Hubeny, I. 1988, *Computer Physics Communications*, 52, 103
- Hubeny, I. 2003, in *PASP*, Vol. 288, *Stellar Atmosphere Modeling*, ed. I. Hubeny, D. Mihalas, & K. Werner, 17
- Hubeny, I., Heap, S. R., & Lanz, T. 1998, in *PASP*, Vol. 131, *Properties of Hot Luminous Stars*, ed. I. Howarth, 108
- Hubeny, I., Hummer, D. G., & Lanz, T. 1994, *A&A*, 282, 151
- Hubeny, I., & Lanz, T. 1995, *ApJ*, 439, 875
- . 2011a, *TLUSTY: Stellar Atmospheres, Accretion Disks, and Spectroscopic Diagnostics*, *Astrophysics Source Code*. <http://ascl.net/1109.021>
- . 2011b, *Synspec: General Spectrum Synthesis Program*, *Astrophysics Source Code*. <http://ascl.net/1109.022>
- Hubeny, I., & Mihalas, D. 2014, *Theory of Stellar Atmospheres* (Princeton, NJ: Princeton Univ. Press)
- Johnson, C., Green, E., Wallace, S., et al. 2014, in *PASP*, Vol. 481, *6th Meeting on Hot Subdwarf Stars and Related Objects*, ed. V. van Grootel, E. Green, G. Fontaine, & S. Charpinet, 153

- Kurucz, R. 1994, Atomic Data for Fe and Ni. Kurucz CD-ROM No. 22. Cambridge, 22
- Kurucz, R. L. 2017, *Canadian Journal of Physics*, 95, 825
- Lanz, T., & Hubeny, I. 1995, *ApJ*, 439, 905
- Lanz, T., & Hubeny, I. 2003, *ApJS*, 146, 417
- . 2007, *ApJS*, 169, 83
- Lanz, T., Hubeny, I., & Heap, S. R. 1997, *ApJL*, 485, 843
- Lei, Z., Zhao, J., Németh, P., & Zhao, G. 2019, *ApJ*, 881, 135
- . 2020, *ApJL*, 889, 117
- Levenhagen, R. S., Diaz, M. P., Coelho, P. R. T., & Hubeny, I. 2017, *ApJS*, 231, 1
- Luo, D., & Pradhan, A. K. 1989, *Journal of Physics B Atomic Molecular Physics*, 22, 3377
- Luo, Y., Németh, P., Deng, L., & Han, Z. 2019, *ApJL*, 881
- Mendoza, C., Eissner, W., LeDourneuf, M., & Zeippen, C. J. 1995, *Journal of Physics B Atomic Molecular Physics*, 28, 3485
- Mihalas, D., & Hummer, D. G. 1974, *ApJS*, 265, 343
- Moehler, S. 2001, *PASP*, 113, 1162, doi: [10.1086/323297](https://doi.org/10.1086/323297)
- Nahar, S. N. 1996, *PhRvA*, 53, 2417
- . 1997, *PhRvA*, 55, 1980
- Nahar, S. N., & Pradhan, A. K. 1993, *Journal of Physics B Atomic Molecular Physics*, 26, 1109
- Nemeth, P. 2019, in *Astronomical Society of the Pacific Conference Series*, Vol. 519, *Radiative Signatures from the Cosmos*, ed. K. Werner, C. Stehle, T. Rauch, & T. Lanz, 117. <https://arxiv.org/abs/1901.04742>
- Németh, P., Kawka, A., & Vennes, S. 2012, *MNRAS*, 427, 2180, doi: [10.1111/j.1365-2966.2012.22009.x](https://doi.org/10.1111/j.1365-2966.2012.22009.x)
- Nemeth, P., Østensen, R., Tremblay, P.-E., & Hubeny, I. 2014, *PASP*, 481
- O’Toole, S. J., & Heber, U. 2006, *A&A*, 452, 579, doi: [10.1051/0004-6361:20053948](https://doi.org/10.1051/0004-6361:20053948)
- Peach, G., Saraph, H. E., & Seaton, M. J. 1988, *Journal of Physics B Atomic Molecular Physics*, 21, 3669
- Pelisolì, I., Vos, J., Geier, S., Schaffenroth, V., & Baran, A. S. 2020, *A&A*, 642, A180
- Rauch, T., Demleitner, M., Hoyer, D., & Werner, K. 2018, *MNRAS*, 475, 3896, doi: [10.1093/mnras/sty056](https://doi.org/10.1093/mnras/sty056)
- Rebassa-Mansergas, A., Parsons, S. G., Dhillon, V. S., et al. 2019, *NatAs*, 3, 553, doi: [10.1038/s41550-019-0746-7](https://doi.org/10.1038/s41550-019-0746-7)
- Saffer, R. A., Green, E. M., & Bowers, T. P. 2001, *PASP*, 47
- Sale, S. E., Schoenaers, C., & Lynas-Gray, A. E. 2008, in *Astronomical Society of the Pacific Conference Series*, Vol. 392, *Hot Subdwarf Stars and Related Objects*, ed. U. Heber, C. S. Jeffery, & R. Napiwotzki, 109
- Schöning, T., & Butler, K. 1989, *A&AS*, 78, 51
- Schwab, J. 2018, *MNRAS*, 476, 5303
- Shamey, L. J. 1969, PhD thesis, University of Colorado at Boulder
- Tremblay, P. E., & Bergeron, P. 2009, *ApJ*, 696, 308
- Tully, J. A., Seaton, M. J., & Berrington, K. A. 1990, *Journal of Physics B Atomic Molecular Physics*, 23, 3811
- Wade, R. A., Stark, M. A., & Green, R. F. 2005, in *Astronomical Society of the Pacific Conference Series*, Vol. 334, *14th European Workshop on White Dwarfs*, ed. D. Koester & S. Moehler, 123
- Willians, R. E., & Livio, M. 1995, *PASP*, 152
- Yi, S., Lee, Y., Woo, J., et al. 1999, *ApJ*, 513, 128